



# Numerical modeling of concentration polarization and inorganic fouling growth in the pressure-driven membrane filtration process



Wende Li<sup>a</sup>, Xu Su<sup>a</sup>, Alan Palazzolo<sup>a,\*</sup>, Shehab Ahmed<sup>b</sup>

<sup>a</sup> Department of Mechanical Engineering, Texas A&M University, College Station, TX 77840, United States

<sup>b</sup> Department of Electrical Engineering, Texas A&M University at Qatar, Doha, Qatar

## ARTICLE INFO

### Keywords:

Concentration polarization  
Inorganic fouling  
Crystal growth  
Lattice Boltzmann method  
Pressure-driven membrane filtration

## ABSTRACT

Concentration polarization and surface fouling may be two of the most remarkable features in the pressure-driven membrane filtration process. A new numerical simulation model is proposed in this paper to study the concentration polarization (CP) and the inorganic fouling growth. The numerical study is based on the lattice Boltzmann method (LBM), which allows a simultaneous solution of the Navier–Stokes equations and the convection-diffusion equation. Simulation results are verified by comparisons with published CP and permeate flux data under the same operating conditions. Then the model is extended to predict CP in a spacer filled desalination channel. The prediction result indicates that there is a higher fouling potential near the spacer filaments due to higher CP values in that area. Coupling of the CP prediction model with gypsum growth kinetics provides an approach to study the inorganic fouling growth on the membrane surface at a single crystal level, with respect to a given solution supersaturation near the membrane surface. Predicted equivalent radius and accumulated mass of the growing gypsum crystal, under the effects of growth retardation by bicarbonate, agree with published test data and analytical results. The presented numerical model enables a direct evaluation of the impacts on the surface crystal development in the presence of antiscalants. This numerical model can be applied to identify suitable operating conditions, assist in dose selection of antiscalants when required properties are available, and predict the fouling mitigation effects in the pressure-driven membrane filtration process.

## 1. Introduction

Countries with limited water resources and rapid population growth are facing an increased fresh water shortage. One effective approach to address the fresh water shortage lies in coordinating water management, water purification, and water conservation [1]. The two most commercially successful water purification techniques include the thermal evaporation and the membrane separation. Pressure-driven membrane separation techniques (e.g. microfiltration (MF), ultrafiltration (UF), nanofiltration (NF), and reverse osmosis (RO)) in particular have been the preferred methods for wastewater treatment and saltwater desalination. By 2010, pressure-driven membrane operations constituted 38%, 87% and 79% of the total water production from seawater, brackish water and wastewater, respectively (by desalination or reclamation) [2]. However, the performance of the pressure-driven membrane separation is still limited by several aspects. These limitations include the operating cost (such as the energy consumption), surface fouling, and membrane replacement. Membrane lifetime and permeate flux are primarily affected by CP and membrane surface

fouling [1]. Some believe that the rapid decline of permeate flux over time as a result of membrane fouling, especially the inorganic fouling [3], is a major obstacle for wide application of the membrane separation approach [4,5]. Membrane fouling causes a reduced productivity, deteriorated permeate quality, increased energy consumption thus higher treatment cost, and a shorter membrane life span [6]. Despite the extensive studies in concentration polarization of fouling formation, the fundamental mechanisms in terms of the fluid dynamics and the mass transport for the CP and the fouling growth are not fully understood.

RO membrane fouling is a complicated problem affected by a number of complex physical and chemical parameters. A. Fane et al. [6] summarized these factors into three categories: feed water characteristics, membrane properties, and hydrodynamic conditions. The inherent CP plays a vital role in triggering the surface fouling, as it leads to elevated solute concentrations near the membrane surface. CP arises when a portion of water solvent passes through the membrane and the rejected solute ions tend to accumulate in the vicinity of the membrane surface. A steady-state concentration gradient will be established when

\* Corresponding author.

E-mail address: [a-palazzolo@tamu.edu](mailto:a-palazzolo@tamu.edu) (A. Palazzolo).

<https://doi.org/10.1016/j.memsci.2018.10.007>

Received 26 July 2017; Received in revised form 30 September 2018; Accepted 7 October 2018

Available online 11 October 2018

0376-7388/ © 2018 Elsevier B.V. All rights reserved.

**Nomenclature**

<b>u</b>	fluid velocity vector, [m/s]	$\nu$	kinematic viscosity ( $\nu = \mu / \rho$ ), [m <sup>2</sup> /s]
<b>C</b>	solute concentration, [kg/m <sup>3</sup> ] or [g/L]	$\mu$	absolute or dynamic viscosity, [(N·s/m <sup>2</sup> )] or [kg/(m·s)]
<b>v<sub>n</sub></b>	volumetric permeate flux normal to membrane wall, [m/s]	$\rho$	density of solution, [kg/m <sup>3</sup> ]
<b>C<sub>w</sub></b>	concentration of solute at the membrane surface, [kg/m <sup>3</sup> ] or [g/L]	$\rho_g$	gypsum crystal effective density, [kg/m <sup>3</sup> ]
<b>C<sub>p</sub></b>	concentrate of solute in the permeate flow, [kg/m <sup>3</sup> ] or [g/L]	<b>D</b>	diffusion coefficient (diffusivity), [m <sup>2</sup> /s]
<b>C<sub>b</sub></b>	concentration of solute in the feed bulk flow, [kg/m <sup>3</sup> ] or [g/L]	<b>k<sub>m</sub></b>	mass transfer coefficient, [m/s]
<b>C<sub>s</sub></b>	saturation concentration at a given temperature, [kg/m <sup>3</sup> ] or [g/L]	<b>H</b>	height of feed channel, [m]
<b>SI</b>	Supersaturation ratio, $SI = C/C_s$	<b>u<sub>0</sub></b>	centerline velocity of the fluid in a plain channel, [m/s]
		<b>Re</b>	Reynolds number, $Re = u_0 H / \nu$
		<b>Sc</b>	Schmidt number, $Sc = \nu / D$
		<b>M</b>	gypsum crystal mass, [kg]
		<b>A<sub>c</sub></b>	single crystal hemispherical surface area, [m <sup>2</sup> ]
		<b>r<sub>eq</sub></b>	equivalent radius of the single crystal coverage area, [m]
		<b>R<sub>sc</sub></b>	node coverage ratio by gypsum crystal

the solute convection process is balanced by the solute back-diffusion process. The development of CP in a membrane channel is affected by the local hydrodynamic conditions and mass transport conditions. Thus, CP depends on operating conditions, and is very difficult to observe experimentally [7]. Thus, numerical prediction of solute CP for specific membrane filtration cases is crucial for the performance prediction and the process improvement [8].

CP has been widely studied for the pressure-driven membrane separation processes. The stagnant film model (or the classical film theory) provided a straight explanation of the concentration polarization phenomenon [9]. However, in the film theory, the assumption of a uniform CP layer and invariant permeate flux along the filtration channel is not accurate for the cross-flow membrane filtration, where the CP layer develops gradually along the filtration channel. Also, the constant flux assumption would lead to significant errors in the CP simulation [10]. In later work, the solute transport equation involving convection and diffusion was solved in a whole channel by numerical methods such as the finite difference method [7,10] and the finite element method [11]. However, these works employed simplified laminar velocity profiles in a channel with porous walls solved by Berman [12]. Thus, the detailed interactions of momentum and mass transfer in separation processes were not adequately simulated. The presence of feed spacers (or so-called turbulence promoters) in a feed parallel-wall channel apparently requires special attention. It has been reported in the literature [13] that the spacers can significantly alter the hydrodynamic conditions and mass transfer patterns in a membrane filtration channel. Commercial computational fluid dynamics (CFD) software has been applied as a rigorous tool to describe the concentration polarization and the influence of the spacer configurations. The main advantage of CFD software lies in its ability to represent the hydrodynamics and the mass transfer properties in complex system geometries through the use of the finite element or the finite volume numerical approaches [14,15]. Presently, enormous improvements in the computational methods facilitate the developing of more flexible and advanced numerical algorithms that surpass commercial CFD software for solving complex hydrodynamics and mass transfer problems. Ma and Song [16] developed a 2-D streamline upwind Petrov/Galerkin finite element model for numerically solving the coupled convection-diffusion equation and the Navier-Stokes equations in the feed channel to predict the CP in the presence of feed spacers. The impact of the spacer filament geometry on CP and permeate flux was further studied by Song and Ma [17] based on the same model. J. Kromkamp et. al first developed a numerical model using the lattice Boltzmann method to simulate the hydrodynamics of a suspension flow and the CP in cross-flow microfiltration [18]. This study assumed that the suspended particles are fully retained by the membrane by applying non-flux conditions on the membrane. However, this study didn't consider the spacer filaments in the microfiltration process. In the present work, a new LBM CP

prediction model is developed with spacer filaments considered. Effective yet simple boundary conditions for the Navier–Stokes equations and the convection-diffusion equation in a typical membrane filtration channel are adopted, and some special treatments for solving the large Peclet number problem in an ion convection-diffusion process are also introduced in this paper.

Inorganic fouling growth is often a slow kinetic process, and the development of scale mitigation strategies typically relies on thermodynamic solubility calculations and experimental trial and error. Visual inspection and microscopy are direct methods used to evaluate the extent of inorganic fouling in certain operating conditions and to check the effects of fouling mitigation strategies, though they require disassembly of the test modules. Y. Cohen etc. developed a visual inspection method to study the gypsum scale formation in a plate-and-frame RO module via the flux decline measurement and the membrane surface imaging [19]. In a later study [20], Y. Cohen etc. extended this crystal growth visual observation method to experimentally quantify mineral scale nucleation and growth on RO membranes aiming to compare the effects of antiscalants in retarding the mineral scale formation. However, this direct observation method was severely constrained by the module dimensions, such as the membrane surface area, membrane length, and channel height, thus it may not be effective as a prediction tool for other desalination systems. Also, the development of the hardware module, as well as the membrane destruction test feature of this method may cause it to be uneconomical. Furthermore, the fouling attachment is disturbed during the disassembly, thus the accuracy of this observation method could be reduced. Although a non-destructive RO ex-situ scale observation detector (EXSOD), consisting of a plate-and-frame RO cell with an optical window, an optical microscope and a high-resolution digital camera, was developed for direct visual real-time monitoring of mineral surface scaling on RO membranes [21], a comprehensive understanding of the causes and consequences of fouling formation is still evolving in experimental scaling studies. These measurements and observations also do not provide any dynamic results, such as the fluid dynamics and the concentration distributions, instead yielding only the fouling attachment. Numerical modeling should be an effective and economical method for the direct simulation of fouling growth and the characterization of the local flow and concentration fields. Radu and Picioreanu [22] developed a two-dimensional mathematical model integrating fluid flow and solutes mass transport for crystal nucleation and growth to study gypsum (CaSO<sub>4</sub>·2H<sub>2</sub>O) scaling in spacer filled membrane feed channels. The thickness of the outer layer of scaling during precipitate expansion is tuned by fitting experimental data while the inner precipitate layer does not grow. The study focused on the crystal mass accumulation on a 2-D cross-section (perpendicular to the channel plates) of the feed channel, while the expansion form and growth of gypsum fouling on the membrane surface (parallel to the channel plates) was not addressed.

M. Johns performed a 3-D simulation of biofilm growth in porous media [23], which showed a promising applicability of the lattice Boltzmann method in mass transport problems. However, the literatures involving the modeling and prediction of the inorganic fouling growth on a pressure-driven membrane surface to facilitate a direct fouling simulation and visualization are still very limited. In the present work the developed CP prediction model based on the lattice Boltzmann method is successfully extended by coupling the gypsum growing kinetics with the predicted hydrodynamic and mass transport fields to study the inorganic fouling growth on the membrane surface. This novel numerical model can be used to aid in the design of filtration conditions and the dose selection/optimization of antiscalants for fouling mitigation, since a direct fouling growth prediction could be a better indication of the degree of membrane degradation.

## 2. The membrane filtration process modeling with the lattice Boltzmann method

### 2.1. Development of LBM scheme

Two sets of particle distribution functions (PDFs) are employed to simulate the convection-diffusion process of salt water in an incompressible flow. One PDF is for solving the flow dynamics and another PDF is for solving the solute mass transport. The evolution of the distribution functions is governed by the following lattice Boltzmann equations containing collision and streaming [24,25]:

$$\begin{cases} f_i(\mathbf{x} + \mathbf{e}_i\delta t, t + \delta t) - f_i(\mathbf{x}, t) = -\frac{1}{\tau} [f_i(\mathbf{x}, t) - f_i^{eq}(\mathbf{x}, t)] \\ g_i(\mathbf{x} + \mathbf{e}_i\delta t, t + \delta t) - g_i(\mathbf{x}, t) = -\frac{1}{\tau_s} [g_i(\mathbf{x}, t) - g_i^{eq}(\mathbf{x}, t)] \end{cases} \quad (1)$$

where  $f_i(\mathbf{x}, t)$  and  $g_i(\mathbf{x}, t)$  are the distribution functions for the fluid and concentration fields at position  $\mathbf{x}$  and time  $t$ , respectively. The subscript  $i$  indicates the lattice direction,  $\delta t$  is the time increment,  $\tau$  and  $\tau_s$  are the non-dimensional relaxation times,  $\mathbf{e}_i$  denote lattice velocities and  $f_i^{eq}$  and  $g_i^{eq}$  are the equilibrium distribution functions (EDFs). The kinematic viscosity  $\nu$  of the fluid and the mass diffusivity  $D$  (diffusion coefficient) are related to the dimensionless relaxation time by Eq. (2) [24]

$$\begin{cases} \nu = (\tau - 1/2)c^2\delta t/3 \\ D = (\tau_s - 1/2)c^2\delta t/3 \end{cases} \quad (2)$$

The EDFs must be defined appropriately so that the mass and momentum are conserved [26]. The local equilibrium distribution functions are defined by Eq. (3) [27] in order to recover the correct NS equations and the convection-diffusion equation,

$$\begin{cases} f_i^{eq} = w_i\rho \left[ 1 + \frac{\mathbf{e}_i \cdot \mathbf{u}}{c_s^2} + \frac{(\mathbf{e}_i \cdot \mathbf{u})^2}{2c_s^4} - \frac{\mathbf{u} \cdot \mathbf{u}}{2c_s^2} \right] \\ g_i^{eq} = w_i C \left[ 1 + \frac{\mathbf{e}_i \cdot \mathbf{u}}{c_s^2} \right] \end{cases} \quad (3)$$

where  $\mathbf{u}$  is fluid velocity,  $\rho$  is fluid density,  $C$  is solute concentration, and  $w_i$  is the weight coefficients. Here  $c_s = c/\sqrt{3}$  is the lattice sound speed, in which  $c = \delta x/\delta t = 1$  for a standard square lattice, and  $\delta x = 1$  is the lattice spacing. The weights are given by  $w_0 = 4/9$ ,  $w_i = 1/9$  for  $i = 1-4$ ,  $w_i = 1/36$  for  $i = 5-8$ . For the D2Q9 (2 dimensions and 9 velocity vectors) LBM, the discrete velocities  $\mathbf{e}_i$  are given by:

$$\mathbf{e}_i = \begin{cases} (0, 0) & i = 0 \\ c\{\cos[(i-1)\pi/2], \sin[(i-1)\pi/2]\} & i = 1, 2, 3, 4 \\ \sqrt{2}c\{\cos[(2i-9)\pi/4], \sin[(2i-9)\pi/4]\} & i = 5, 6, 7, 8 \end{cases} \quad (4)$$

The macroscopic properties, including the fluid density  $\rho$ , flow velocity  $\mathbf{u}$ , flow pressure  $P$ , and mass concentration  $C$ , are readily available from the PDFs as

$$\rho = \sum_{i=0}^8 f_i, \quad \mathbf{u} = \frac{1}{\rho} \sum_{i=0}^8 \mathbf{e}_i f_i, \quad P = c_s^2 \rho, \quad C = \sum_{i=0}^8 g_i \quad (5)$$

The Navier-Stokes equations (NSE) describing the macroscopic flow and the convection-diffusion equation (CDE) describing the solute transport can be recovered from the equilibrium distribution functions shown in Eq. (3) via the Chapman-Enskog analysis with a second-order accuracy [28,29]. The LBM is alternative numerical approach for solving the governing equations (NSE and CDE), and the simulation domain as well as the boundary are discretized into a mesh of nodes similar to the finite element method or the finite difference method. The distribution functions are solved for at each node by a collision process and a streaming process, the then the distribution functions are used to calculate the macroscopic parameters shown in in Eq. (5).

### 2.2. Model setup and boundary conditions

The geometry of the spacer filled feed channel in the pressure-driven membrane filtration process and the applied boundary conditions are illustrated in Fig. 1. Boundary conditions are fundamental in LBM simulations, which usually determine the efficiency of the calculation and the accuracy of the result. Boundary schemes in LBM for the fluid dynamics and the mass transport are applied separately for each boundary. The distribution functions  $\phi_i$  in Fig. 1 denote  $f_i$  for the fluid field or  $g_i$  for the concentration field.

#### 2.2.1. Simulation model setup

The height of the desalination channel shown is set to be 1 mm, the diameter of the spacer filament is set to be 0.5 mm, the distance between adjacent spacer filaments is set to be 2.5 mm, and the distance between the centers of the cylindrical filament to the nearest membrane are set to be 0.3 mm. Actually the spacer filaments are not in touch with the membrane but there is a 0.05 mm gap between them. This treatment is reasonable since although the knots on the spacer should be compressed by the membrane in the feed channel, there is still flow around the main body of the filaments. Also, the spacer filaments are not uniform cylinders but complex geometries [30]. So, in the present

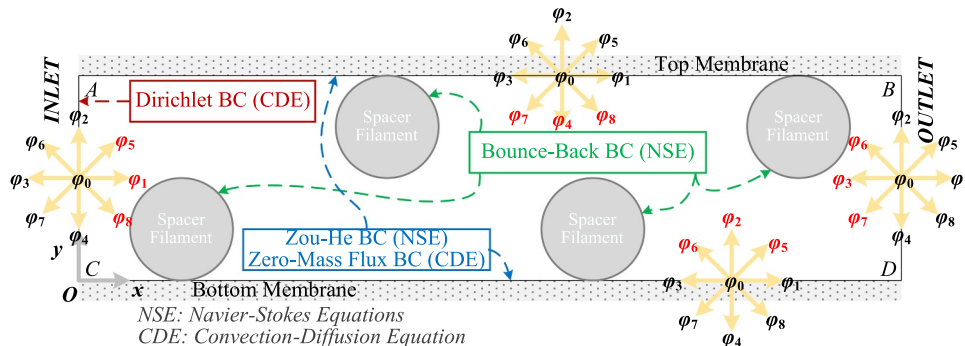


Fig. 1. Fluid Dynamics and Mass Transport Boundary Conditions.

study, the filaments are simplified as circles but are separated from the membrane walls with 0.05 mm offset centers.

### 2.2.2. Boundary conditions for the Navier-Stokes equations

The known velocity boundary condition is applied on the bottom and top membrane boundaries by a Zou-He boundary scheme [31] to prescribe the permeate flux through the membranes. The tangential velocity on the bottom and top boundaries is set as zero to meet the no-slip condition. The vertical velocity normal to the bottom and top boundaries is set equal to the permeate flux calculated by  $v_w = P_{er}(\Delta P - \Delta\pi)$ , in which  $P_{er}$  is the permeability constant of the RO membrane,  $\Delta P$  is the applied pressure, and  $\Delta\pi$  is the osmotic pressure between the feed side and the permeate side of the membranes. A simple bounce-back scheme is used to achieve the no-slip boundary condition at the circumference of the spacer filaments. Bounce-back scheme refers to when the fluid particles reach a boundary node, the particles scatter back to the fluid along with their incoming directions. Following bounce-back scheme, the unknown populations in post-streaming form on the boundary can be calculated by

$$f_i^+(\mathbf{x}_b, t + \delta t) = f_i^+(\mathbf{x}_b, t) \quad (6)$$

where  $f_i^+$  are the known distribution functions in post-collision form.

The flow in the desalination channel (with or without spacers) is driven by a pressure gradient ( $G = -\partial p/\partial x$ , in a unit of  $N/m^3$ ), which can be achieved by adding a body force density term (still in a unit of  $N/m^3$ ) in LBM following Z. Guo's method [32].

### 2.2.3. Boundary conditions for the convection-diffusion equation

In a pressure-driven membrane filtration process, the solute is assumed to be totally blocked by the membrane. Although the total mass flux is zero on the boundary in this process, there is flow (or permeate flux) through the membrane boundary. A suitable treatment of such a boundary is to admit the existence of the convection flux near the boundary, and consider a back transport of the solute to the bulk flow, which is called back-diffusion (where the total flux is still zero) [33]. Such a zero-flux treatment will reasonably induce a solute concentration gradient and an accumulation of the solute near the boundary layer (concentration polarization). M. Yoshino [27] proposed a zero-flux boundary scheme based on an assumption that the normal mass flux of  $\sigma$ -species is zero on the boundary nodes, and then the desired unknown wall concentration on the boundary,  $C_w$ , is specified by:

$$C_w = -\frac{\sum_{i(\mathbf{e}_i \cdot \mathbf{n} \leq 0)} g_i \mathbf{e}_i \cdot \mathbf{n}}{\sum_{i(\mathbf{e}_i \cdot \mathbf{n} > 0)} w_i \mathbf{e}_i \cdot \mathbf{n}} \quad (7)$$

M. Yoshino [27] proposed an approximation method for the unknown distribution functions using the calculated wall concentration  $C_w$ , as

$$g_i = w_i C_w \quad \text{for } \mathbf{e}_i \cdot \mathbf{n} > 0 \quad (8)$$

Thus, the calculated wall concentration  $C_w$  on the boundary from Eq. (7) will be used to calculate the unknown distribution functions by Eq. (8). Taking the straight boundary in Fig. 2 as an example, the unknown wall concentration can be calculated by

$$C_w = \frac{g_4 + g_7 + g_8}{w_2 + w_5 + w_6} \quad (9)$$

With the calculated  $C_w$  on the bottom membrane surface, the unknown distribution functions  $g_2, g_5$  and  $g_6$  can be obtained by Eq. (8). Similar procedures can be applied to calculate the unknown distribution functions on the top membrane boundary.

Note that the bounce-back scheme for mass transport is another boundary treatment only valid for the zero-flux boundary, which mimics the no-slip boundary condition in solving NS equations [34]. The zero-flux boundary condition should also be prescribed for the cylindrical spacer filaments in the desalination channel shown in Fig. 1.

However, the zero-flux boundary is ignored in this paper for improved computational stability. This approach will result in only a small amount of diffusion flux through these filament areas, since there is no convection flux in these areas (the bounce-back or no-slip boundary is applied for the fluid). The small diffusion flux in the filament areas can be ignored when it is compared to the much larger convection flux in the bulk flow [35].

### 2.2.4. Treatment for the large Peclet number convection-diffusion processes

In many mass transport cases, small particles such as ions in dilute solution have very small diffusion coefficient. For example, the self-diffusion coefficients of the five major ions in seawater at 25 °C are all in the order of  $1 \times 10^{-9}$  ( $m^2/s$ ) [36]. Following the unit conversion procedures in Appendix A, the solute relaxation time can be calculated by,

$$D_{LBM} = (\tau_s - 1/2)c^2\delta t/3 \xrightarrow{c=1, \delta t=1} \tau_s = 3D_{LBM} + 1/2 \quad (10)$$

The calculated relaxation time is  $\tau_s = 0.5008$  when using a diffusion coefficient  $D = D_{PHY} = 1.5 \times 10^{-9}$   $m^2/s$ , which is near the instability value of 0.5 in lattice Boltzmann method. Sometimes, in a coupled simulation of the Navier-Stokes equations and the convection-diffusion equation, the correlated values between the fluid field relaxation time  $\tau$  and the concentration field relaxation time  $\tau_s$  should be strictly controlled to accurately represent the ratio of the convective mass transport to the diffusive mass transport. Peclet number is defined as the ratio of the rate of advection of a physical quantity by the flow to the rate of diffusion of the same quantity driven by an appropriate gradient, as

$$Pe = \frac{Lu}{D} = \frac{Lu}{\nu} \cdot \frac{\nu}{D} = Re \cdot Sc \quad (11)$$

In this case,  $\nu$  is the kinematic viscosity. Take seawater for an example,  $\nu = 1 \times 10^{-6}$  ( $m^2/s$ ), thus the calculated  $Sc \approx 667$ . For a channel flow with  $Re = 100$ , the Peclet number is  $Pe \approx 66,700$ . For such a large Peclet number problem, the diffusion is usually ignored in the fluid flow direction. However, in other cases, such as membrane filtration process and mass transport in porous media, although the mass in the bulk flow is convection dominated, on the boundary layer, the diffusion plays an important role since the permeate flow induced convection is comparable with the mass gradient-induced diffusion. Thus, the coupled simulation of such a complex convection-diffusion process suffers computational stability problems with regular LBM routines. J. Perko developed an effective lattice Boltzmann scheme for advection-diffusion problems with large diffusion-coefficient heterogeneities and high-advection transport [37]. The basic idea is to divide the physical diffusion coefficient into a reference value  $D_{ref}$ , which is constant over the entire domain, and a fluctuating or residue value  $\hat{D}$ , which represents a deviation from the reference ( $D = D_{ref} + \hat{D}$ ). A diffusion velocity  $\mathbf{u}_d$  is introduced by transferring the fluctuating diffusion

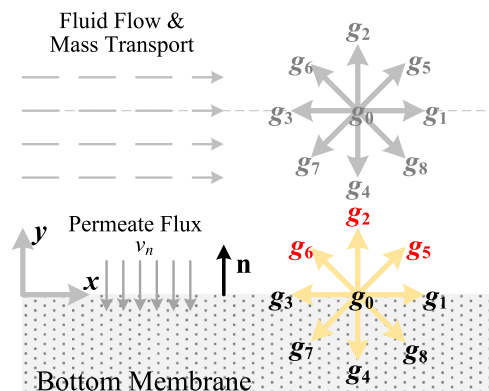


Fig. 2. Boundary Conditions at the Bottom Membrane Surface.

part to an advection term, as

$$\mathbf{J} = \mathbf{u}C - (D_{ref} + \hat{D})\nabla C = -D_{ref}\nabla C + (\mathbf{u} + \mathbf{u}_d)C \quad (12)$$

In Eq. (12),

$$\mathbf{u}_d = -\frac{\hat{D}\nabla C}{C} \quad (13)$$

For a large Peclet number problem with a very small physical diffusion coefficient, the reference diffusion coefficient can be selected to be a large value for better stability ( $D_{ref}=50D$  in this paper), and in this case the residue diffusion part should be negative.

### 2.2.5. The reaction boundary for fouling growth

The simulation of the crystal growth involves the reaction between gypsum crystals and the surrounding solution. A first-order kinetic-reaction model at the fluid-solid interface is adopted in this paper, as

$$D\partial C/\partial \mathbf{n} = k_r(C - C_s) \quad (14)$$

in which  $D$  is the diffusivity,  $C$  is the concentration at the interface,  $C_s$  is the concentration at saturation,  $k_r$  is the local reaction-rate constant, and  $\mathbf{n}$  is the direction normal to the interface. Q. Kang [38] proposed an observation that at a stationary wall, the non-equilibrium portion of the distribution function is proportional to the dot product of the function's microscopic velocity and the concentration gradient. Thus, the solute concentration at the boundary nodes as illustrated in Fig. 2 can be calculated by

$$C_w = (g_4 + \beta C_s)/(w_4 + \beta) \quad (15)$$

where  $\beta = k_r/(8D)$ . Note that the unknown distribution functions are approximated differently in this reaction boundary scheme compared to the approximation method in Eq. (8) in the zero-flux boundary scheme. For example, the unknown distribution functions  $g_2$ ,  $g_5$  and  $g_6$  for a bottom reaction boundary in Fig. 2 should be calculated by:  $g_2 = (2/9)C_w g_4$ ;  $g_5 = (1/18)C_w g_7$ ;  $g_6 = (1/18)C_w g_8$ . Detailed explanation of this approximation method can be found in Ref. [38].

## 3. Results and discussion

### 3.1. Concentration polarization in a plain channel

A benchmark model is selected for the verification purpose. L. Song et al. [17] developed a finite element model for the CP prediction in spiral wound membrane modules, in which both the salt transport and the hydrodynamics can be simultaneously solved either in a plain channel or in a channel filled with spacer filaments. In this paper, the parameters used in the CP prediction for the plain channel are set the same as reference [17]. The LBM approach is used on a cross-section domain ( $H \times L = 1 \text{ mm} \times 10 \text{ mm}$ ) for the plain channel with the prescribed boundary conditions introduced in Section 2.2. The simulation results for the CP and the permeate flux are shown in Fig. 3.

Three different simulation times are selected (2 s, 4 s, and 8 s), and both the CP and the permeate flux converge to the FEM results. This demonstrates that the settling time of the concentration polarization layer is less than 2 s. The concentration profile in Fig. 3 shows that the CP developed quickly at the initial section of the channel, and then the development becomes slower gradually when approaching the channel end. The simulation domain is selected to be a section of a feed channel to capture the initial fast-developing feature of the concentration polarization, while a more gradual-developing CP can be expected for the remainder of the feed channel.

The CP development with different Reynolds numbers can be seen in Fig. 4. A reduced CP and an increased permeate flux can be observed in Fig. 4 for a higher Reynolds number feed flow. This can be explained by the observation that in a channel with higher Reynolds number flow, the back-diffusion process tends to be promoted thus the solute accumulation near the membrane surface (CP) is reduced.

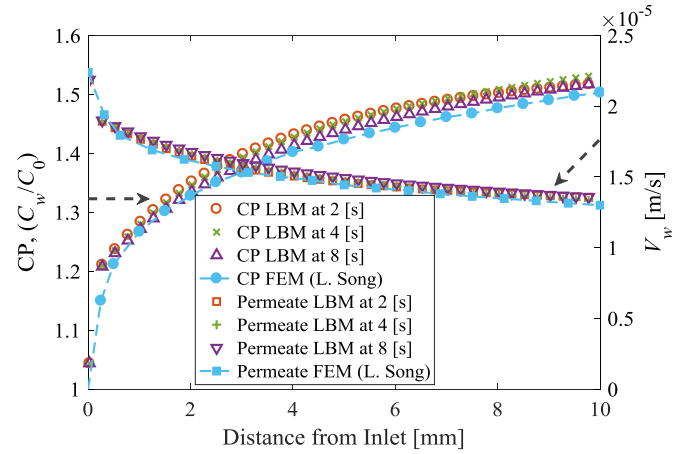


Fig. 3. Concentration Polarization ( $C_w/C_0$ ) and Permeate Flux Profiles in a Plain Channel. Simulation Parameters:  $\Delta p = 800 \text{ psi}$ ;  $C_0 = 32,000 \text{ mg/L}$ ;  $D = 1.5 \times 10^{-9} \text{ m}^2/\text{s}$ ;  $P_{er} = 7.3 \times 10^{-12} \text{ m}/(\text{s}\cdot\text{Pa})$ ;  $u_0 = 0.1 \text{ m/s}$  (Pressure Gradient  $dp/dx = 800 \text{ Pa/m}$  is Applied in the LBM);  $h = 1 \text{ mm}$ .

The thicknesses of the CP boundary layers at the end of the plain channel with flow in different Reynolds numbers can be seen in Fig. 5. The boundary thicknesses for the different Reynolds numbers are very close, which are all about 0.125 mm. But a detailed view in Fig. 5 shows that a higher Reynolds number not only induces a lower CP value but also causes a thinner CP layer thickness.

### 3.2. Concentration polarization in a spacer filled channel

The distribution of the salt concentration can be very complicated when filaments exist. First, consider a comparison case with L. Song's CP [17] prediction model for a channel with spacer filaments only attached to the bottom membrane, in which the computational fluid dynamics was achieved by the finite element method [17]. In the comparison case, the channel height  $h = 1 \text{ mm}$ , the channel length is 12 mm, the diameter of the spacer filaments is  $d = 0.5 \text{ mm}$ , and the spacing between the spacer filaments is  $l_f = 4.5 \text{ mm}$  (Fig. 6).

Comparison of the CP prediction results for this case utilizing the current model and L. Song's [17] model can be seen in Fig. 7. For the unattached side near the top membrane, the CP along the length of the channel drops at the positions of the filaments, this is due to the higher velocities near these positions. For the attached side near the bottom membrane, the predicted CP value at the filament locations by the current model is lower than the prediction by the FEM. This deviation

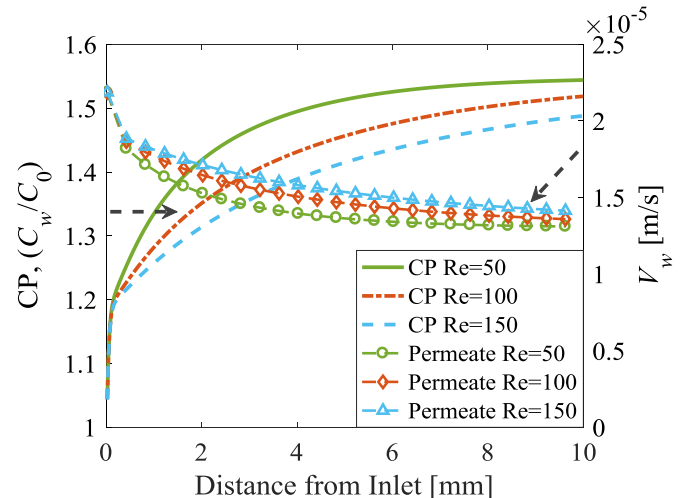


Fig. 4. Concentration Polarization with Different Reynolds Numbers.

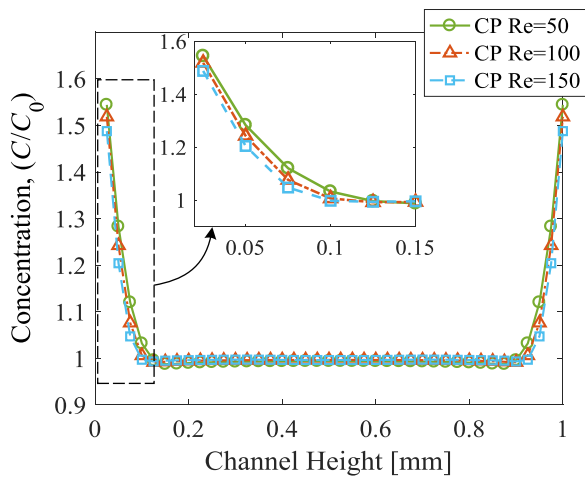


Fig. 5. Concentration Profile and CP Boundary Thickness.

may be explained by in the current model the filaments are actually not in touch with the bottom membrane. This treatment is reasonable since although the knots on the spacer should be compressed by the membrane in the feed channel, there is still flow around the main body of the filament. So, the main body of the filaments should be separated from membrane walls [30].

For the attached side at locations between the two spacer filaments, the current model predicts a higher CP than that by the L. Song's model [17]. From the hydrodynamics shown in Fig. 8, there is no turbulence near the bottom membrane between the two filaments, which indicates a low velocity in this region. Thus, there is no reason for a largely reduced CP as observed in the FEM prediction near the bottom membrane since there is no dramatic increase of the fluid velocity in this region. So, the current CP prediction model provides more reasonable results.

The staggered configuration of the spacer filaments in a desalination channel can be illustrated back to Fig. 1. The diameter of the spacer filament is still set to be 0.5 mm, and the distance between adjacent spacer filaments is set to be 2.5 mm. In this simulation, the distance between the center of the cylindrical filament to the nearest membrane

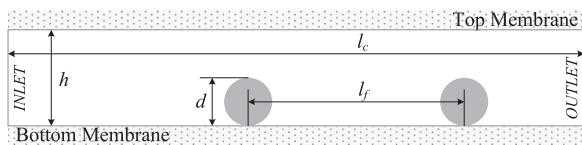


Fig. 6. Geometric Parameters for the Comparison Case.

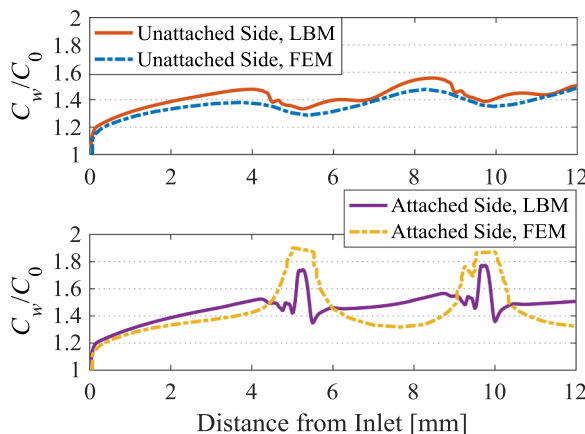


Fig. 7. CP Predictions at the Unattached Side and the Attached Side.

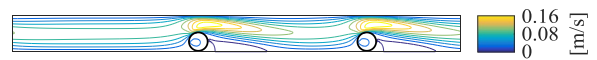


Fig. 8. Hydrodynamics in the Channel for the Comparison Case.

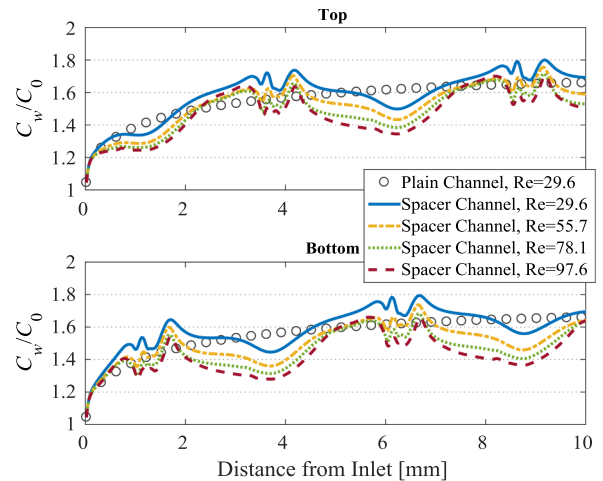


Fig. 9. Concentration Polarization of the Spacer Filled Channel.

is set to be 0.3 mm. Simulation results of the CP prediction in the spacer filled channel with different Reynolds numbers can be seen in Fig. 9. The Reynolds numbers in Fig. 9 are calculated by using the maximum velocities in the channel.

The results show that the CP near the corner of the spacer filaments is higher than that far from the spacer filaments. This is because the fluid velocity around the corner of the spacer is lower than the velocity far from the spacer element. However, the CP value far from the spacer is lower than the plain channel CP value, which is caused by a higher crossflow velocity in the spacer filled channel. The comparison between a plain channel CP and a spacer channel CP with a same Reynolds number (Re = 29.6) shown in Fig. 9 indicates that the plain channel CP is lower than the spacer channel CP at the spacer filament locations. However, at the locations between the spacer filaments along the channel length, the plain channel CP is higher than the spacer channel CP. This can be explained by that the cross-flow velocity between the two spacer filaments along the channel length is increased by the existence of a filaments attached to the membrane at the opposite side. The CP curves shown in Fig. 9 also shows that the maximum CP on the bottom membrane is almost the same as the top membrane for the same Reynolds number, which indicates that the maximum CP in a spacer filled channel is independent of the filament positions along the channel length. A larger CP can be observed in Fig. 9 for a lower cross-flow Reynolds number. The cross-flow velocity in the spacer filled channel with different Reynolds numbers can be seen in Fig. 10.

Fig. 11 is a plot of concentration profile in the spacer filled channel. The rejected solute by the membrane accumulates mainly behind the spacer filaments. This observation conforms to the cross-velocity profile shown in Fig. 10, in which the fluid velocity behind the spacer filaments

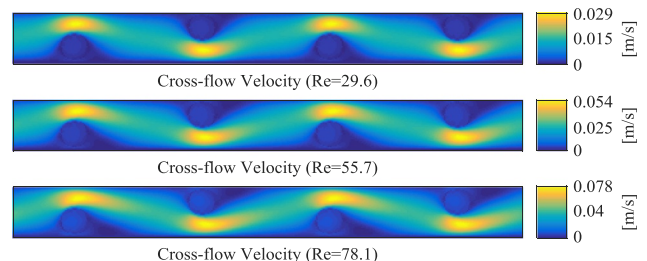


Fig. 10. Cross-flow Velocity Profile in the Spacer Filled Channel.

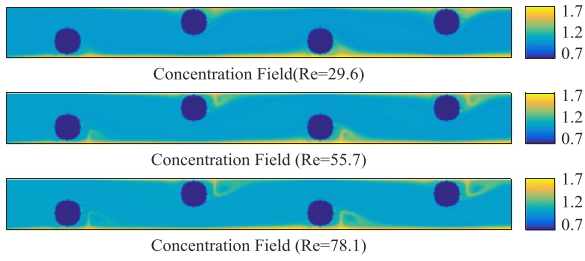


Fig. 11. Concentration Profile in the Spacer Filled Channel.

is lower than that in front of the filaments. A larger Reynolds number reduces the concentration accumulation at this fouling potential area behind the spacer filaments.

LBM differs from other numerical methods involving the computational fluid dynamics such as the finite difference method and the finite element method in that the LBM aims at the distribution and interactions of mesoscopic particles or molecules, thus making it more suitable for representing complex physical phenomena, ranging from multiphase flows to chemical interactions between the fluid and the surroundings. LBM has several advantages over the conventional CFD methods. The nonlinear advection term in the macroscopic approach is replaced by a linear streaming process in LBM. Also, there is no need to solve the Poisson equation at each time step, as is required by the macroscopic CFD approach, to satisfy the continuity equation. This helps reduce the computational time.

### 3.3. The gypsum growth kinetics on the membrane surface

In order to develop effective scale mitigation strategies, there is a need for a direct quantification of the scale formation on the RO membrane surface. The feasibility of a direct and real-time observation of the membrane surface scaling was recently reported [39], but a directly modeling of the membrane surface fouling is difficult for both the traditional numerical methods and the advanced CFD method.

Q. Kang et. al. proposed a lattice Boltzmann model for crystal growth in a supersaturated solution [38], but this model didn't consider the influence of the fluid flow on the growth of the crystal, and the crystal growth scheme is also lattice grid dependent. In the present simulation, a  $2 \times 2 \text{ mm}^2$  membrane surface area is targeted. The top and bottom edges of the simulation area are assumed to be symmetric boundaries. Both hydrodynamic conditions and thermodynamic parameters are set to be the same as those in the CP prediction model, except the pressure gradient  $G = -\partial p / \partial x$  in the feed channel, since the cross-flow velocity near the membrane surface should be lower than the bulk flow velocity. The pressure gradient is set to be 160 (Pa/m) thus the cross-flow velocity near the membrane surface is 0.2 times the

channel centerline velocity  $u_{max}$ .

Calcium sulfate dihydrate (gypsum) is selected as the mineral scalant to demonstrate the proposed approach, given its common occurrence in the desalination of inland or ground brackish water, as well as the tenacity of the formed gypsum scale [20,40]. While calcite scaling can be controlled by pH adjustment, gypsum scaling remains one of the major factors that limits the product water recovery [19]. The current focus is on a direct simulation of the gypsum scale formation at a single crystal level with respect to different solution supersaturation levels on the membrane surface.

Two pathways for the crystallization have been identified [41]: surface (heterogeneous) crystallization and bulk (homogeneous) crystallization. Most of the research indicates that at low supersaturation levels (supersaturation ratio  $SI < 3$ ), the gypsum nucleation mechanism was found to be heterogenous [42,43]. Thus, in this paper, only the dominant surface crystallization mechanism in the pressure-driven membrane filtration process by inorganic salts  $\text{CaSO}_4$  is considered. According to Y. Cohen [39], the growth of a single gypsum crystal on the membrane surface can be described by the standard diffusion gypsum growth kinetics:

$$\frac{dM}{dt} = k_m A_s (C - C_s) \quad (16)$$

where  $M$  is the gypsum crystal mass,  $A_s$  is the single crystal surface area in contact with the solution,  $C$  and  $C_s$  are the concentrations in solution and at saturation, respectively, and  $k_m$  is the solution mass transfer coefficient in crystal growth. Eq. (16) shows that the growth of the gypsum crystal mass, at a given solution saturation with respect to the gypsum (i.e.,  $SI_g$ ), is directly proportional to the gypsum crystal surface area. Also, the surface gypsum crystal actually grows into a rosette structure, and this morphology was reported in [39] on RO membranes. A hemispherical geometry is taken to represent the gypsum rosettes, thus, from Eq. (16),

$$\frac{dM}{dt} = \frac{d\left(\frac{2}{3}\pi r_{eq}^3 \rho_g\right)}{dt} = 2\pi \rho_g r_{eq}^2 \frac{dr_{eq}}{dt} = k_m \cdot 2\pi r_{eq}^2 (C - C_s) \quad (17)$$

where  $r_{eq}$  is the equivalent radius of the single crystal coverage area,  $\rho_g$  is the gypsum crystal effective density. Thus, the gypsum crystal growth equation is given by,

$$\frac{dr_{eq}}{dt} = \frac{k_m}{\rho_g} (C - C_s) \quad (18)$$

D. Hasson [44] proposed that the radial growth of the gypsum crystals is described by the widely adopted kinetic expression:

$$\rho_g \frac{dr}{dt} = k (C_w - C_s)^n \quad (19)$$

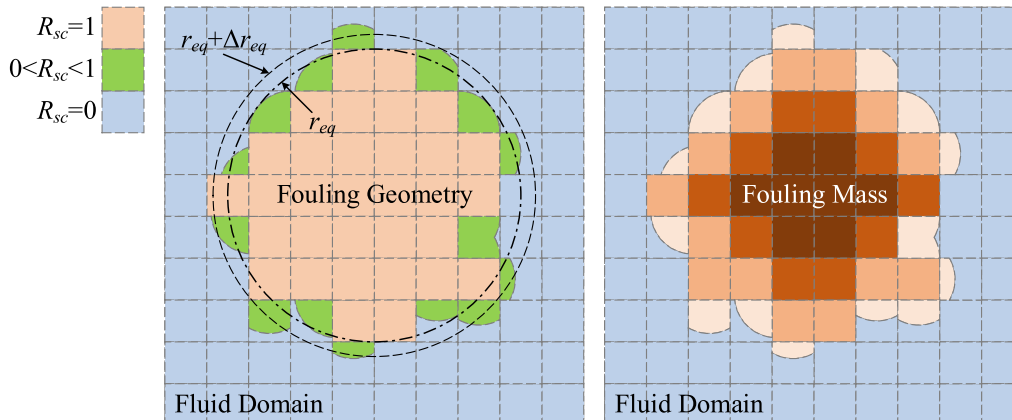


Fig. 12. Growth of the Fouling Geometry and the Fouling Mass.

where  $C_w$  is the solute mass concentration at the membrane surface,  $k$  is the crystallization rate coefficient and  $n$  is the order of the kinetic equation. The value of  $n$  is either 1 or 2 [2,44]. When the crystallization process is diffusion controlled,  $n = 1$  and  $k = k_m$  (mass transfer coefficient in crystal growth). When the crystallization process is controlled by a surface reaction,  $n = 2$  and  $k = k_r$  (surface integration rate coefficient). It should be noted that S. Lee et. al and Y. Cohen et. al [20,45] stated that  $\text{CaSO}_4$  crystallization in the crossflow membrane system follows a first-order equation ( $n = 1$ ). Thus, the current crystal growth equation should be the same as D. Hasson's kinetic expression. The following section will discuss how to implement the crystal growth in the LBM scheme based on the current gypsum crystal growth equation.

### 3.4. Implementation of crystal growth model in LBM

A new node number independent crystal growth implementation scheme is developed in the LBM for the direct evaluation and quantification of crystal growth radius and mass. If a constant mass transfer coefficient  $k_m$  is supposed, then the rate of surface crystallization is directly proportional to the membrane wall concentration of  $\text{CaSO}_4$  salts [45], and the crystal radius growth becomes

$$\Delta r_{eq} = \frac{k_m}{\rho} (C_w - C_s) \Delta t \quad (20)$$

The saturation concentration  $C_s$  of calcium sulfate at a given temperature can be estimated using the expression [46]:

$$C_s = (1846 + 9T) \times 10^{-3}, \quad 15 \leq T \leq 30 \text{ } ^\circ\text{C} \quad (21)$$

A solution temperature of  $T = 25 \text{ } ^\circ\text{C}$  is used in the saturation concentration calculation. The membrane surface concentration is given by  $C_w = SI \times C_s$ , in which  $SI$  is the supersaturation ratio and  $C_s$  is the saturation concentration at a given temperature (with a unit of  $\text{kg}/\text{m}^3$  or  $\text{g}/\text{L}$ ). Since the crystal growth in LBM may not necessarily be a circle, an equivalent radius  $r_{eq}$  is used to transform the arbitrary shape into a circle form, as seen in Fig. 12.

A node coverage ratio by gypsum crystal  $R_{sc}$  is defined to record the radius growth of the crystal.

$$R_{sc}: \begin{cases} = 1, & \text{fully covered} \\ > 0 \text{ and } < 1, & \text{partially covered, growing} \\ = 0, & \text{not covered} \end{cases} \quad (22)$$

The value of  $R_{sc}$  for the partially covered node (or boundary nodes, shown as the light green area in Fig. 12) will increase in each time step by  $\Delta r_{eq}$ . The boundary nodes may not necessarily be at the boundary; they actually include all the partially covered and still growing nodes. A fully covered node, although at the boundary, will not contribute to the radius growth, but mass increase is still occurring (In Fig. 12, a darker color indicates a larger fouling mass). Once a partially covered node becomes a fully covered node, one of the nearest liquid nodes becomes a solid particle, which is also a new partially covered node, following Q. Kang's crystal node expansion scheme [38]. At each time step, the grown portion of the fouling mass  $\Delta m_{eq}$  is distributed equally to all solid fouling nodes including the fully covered interior nodes and the partially covered boundary nodes. The developed node number independent LBM implementation scheme is capable of predicting the crystal morphology and quantifying the crystal growth radius and mass.

### 3.5. Crystal growth simulation results and experimental comparison

The initial plate-like gypsum crystals grow radially outward from the growth centers, forming rosette structures that block the permeation areas of the membrane. To validate the proposed gypsum crystal growth model and the LBM implementation, results the experimental study by Y. Cohen [47] about the influence of bicarbonate on membrane gypsum scaling are used for comparison. In Y. Cohen's study,

bicarbonate concentration was varied ( $\text{HCO}_3^- \leq 7.81 \text{ mM}$ ) for a fixed initial gypsum saturation index (at the membrane surface) of 2.0. The time evolutions of the crystal rosettes clearly demonstrate that there was a remarkable retardation of the gypsum scale growth with the increase of the bicarbonate concentration. The experimental data of the crystal rosettes radius under different bicarbonate concentration is used to compare with simulation results from the developed inorganic fouling growth model. In the experimental study [47], a linear growth of the crystal rosettes with time was observed, thus, the experimental data is linearly fitted to obtain the mass transfer coefficient in Eq. (20) based on the proposed method in [39]. The calculated mass transfer coefficient is  $2.949 \times 10^{-5} \text{ (m/s)}$ , which is located in the range of  $1.4 \times 10^{-5} - 8.1 \times 10^{-5} \text{ (m/s)}$  estimated under operating conditions in [20,47] using a mass transfer coefficient estimation method in [48]. The size of a nucleus originated by the primary nucleation is usually less than  $10^{-8} \text{ m}$  [49], so in this paper, the initial equivalent radius of the nucleus is set as  $1 \times 10^{-8} \text{ m}$ . The initial mass of the nucleus is estimated using a gypsum crystal density of  $2310 \text{ kg}/\text{m}^3$ .

In the first study, the gypsum crystal growth is performed in the absence of the bicarbonate and with a  $\text{CaSO}_4$  supersaturation ratio of 2. The gypsum crystal growth and mass distribution on the membrane surface can be seen in Fig. 13. Simulation results conform to the rosette structure hypothesis and readily provide the crystal size and mass information. The dashed cross lines in Fig. 13 show the initial nucleation positions, which clearly indicate that the crystal is more prone to grow in the countercurrent direction of the feed flow (flow direction is from left to right). This conforms to the experimental observations [39] shown in Fig. 14, in which the axially asymmetric growth of a gypsum crystal is more prone in the direction opposite to that of the feed flow. This phenomenon could be explained by the local fluid and concentration simulation results, shown in Figs. 15 and 16, that the salt concentration decreases from the crystal frontal flow-stagnation edge to the rear of the crystal, and higher concentration induces faster growth in the direction opposite to the feed flow.

Fig. 15 also shows that the formed crystal scaling on the membrane surface acts as a solid obstacle that affects the local cross-flow velocity due to the applied no-slip boundary around the crystal.

Fig. 16 shows that the inorganic salt concentration layer around the crystal scaling is lower than the concentration in the bulk flow. This may be because that the gypsum crystallization process gradually consumes the salt ions around the crystal. Also, the salt concentration decreases from the crystal frontal flow-stagnation edge to the rear of the crystal, which induces the asymmetric structure of the gypsum crystal

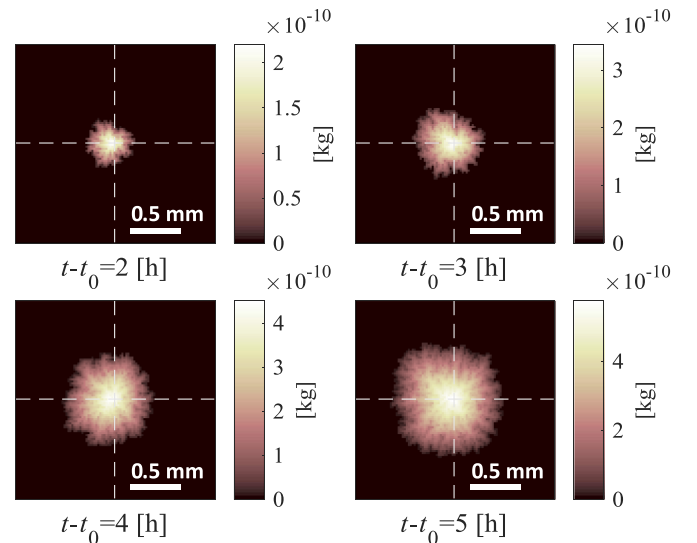


Fig. 13. Crystal Growth and Mass Accumulation on the Membrane Surface.

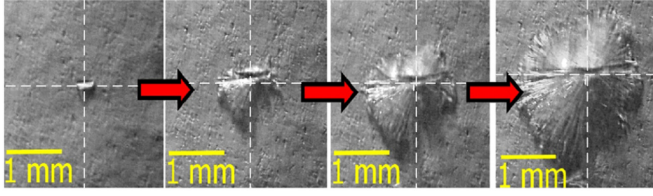


Fig. 14. Illustration of the Asymmetric Growth for the Gypsum Crystal (SI = 1.43) [39].

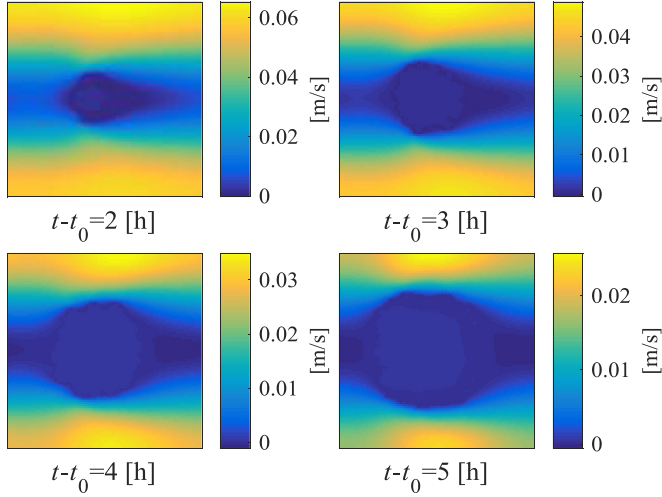


Fig. 15. Cross-flow Velocity around the Crystal Rosette.

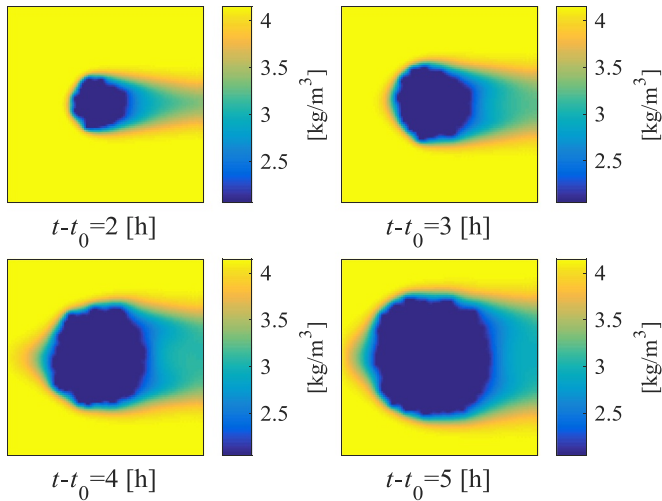


Fig. 16. Solution Concentration around the Crystal Rosette.

rosette. The reduced calcium sulfate concentration downstream of the crystal growth center results from the mixing eddies caused by abrupt obstacle of the growing non-permeation crystal.

In Y. Cohen's test results, a linear growth of crystal rosettes with time was observed with a nearly constant rate that decreased with rising bicarbonate concentration [47]. Bicarbonate adsorption was assumed as a plausible explanation for the observed gypsum scale retardation following the Langmuir isotherm. For the growth of gypsum crystal rosettes on RO membranes, the relevant Langmuir adsorption isotherm for a monolayer of bicarbonate adsorbed onto the gypsum crystal surface can be represented by

$$\Theta = \frac{K_A [\text{HCO}_3^-]_{\text{lm}}^T}{1 + K_A [\text{HCO}_3^-]_{\text{lm}}^T} \quad (23)$$

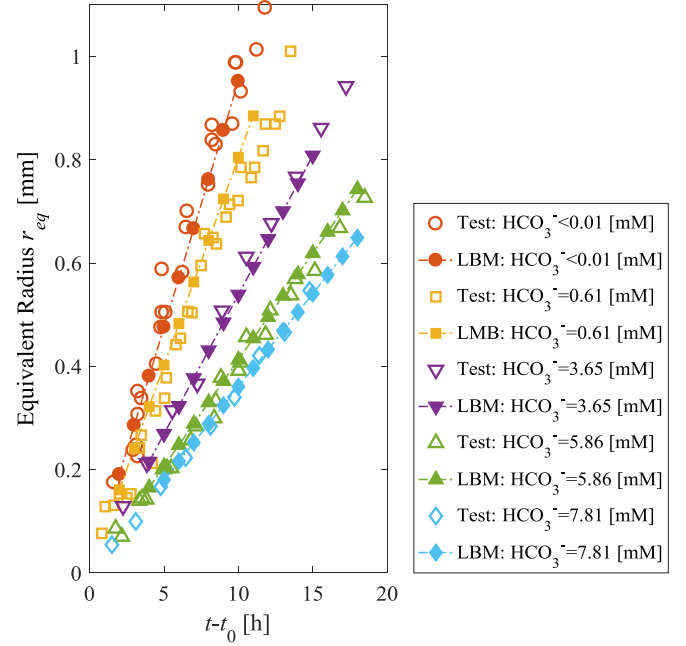


Fig. 17. Comparison of the Equivalent Radius in LBM with Test Data.

where  $\Theta$  is the fraction of crystal surface area occupied by the bicarbonate adsorbed layer,  $[\text{HCO}_3^-]_{\text{lm}}^T$  is the local bicarbonate concentration at the membrane surface (mM), and  $K_A$  is the adsorption equilibrium constant ( $\text{mM}^{-1}$ ). From Eq. (16), the growth of the gypsum crystal mass is directly proportional to the gypsum crystal surface area at a given solution supersaturation. Therefore, one can derive the rate of the crystal rosette radius growth by

$$\frac{dr'_{eq}}{dt} = (1 - \Theta) \frac{k_m}{\rho_g} (C - C_s) = (1 - \Theta) \frac{dr_{eq}}{dt} \quad (24)$$

in which  $(1 - \Theta)$  is the fraction of the gypsum surface area free of bicarbonate.

Fig. 17 shows the comparison of the simulation results and the test data in terms of the gypsum crystal equivalent radius with time under different bicarbonate concentrations. The mass transfer coefficient in the crystal growth model Eq. (16) for all bicarbonate cases is set the same ( $2.949 \times 10^{-5}$  m/s) as the case without the bicarbonate ( $\text{HCO}_3^- < 0.01$  mM). The adsorption equilibrium constant  $K_A$  is set to be  $0.25 \pm 0.05 \text{ mM}^{-1}$  for all bicarbonate cases [47]. Simulation results by the LBM agree well with test data, which indicates a stronger gypsum scaling retardation with increased dosage of the bicarbonate. Also, the LBM simulation based on the Langmuir adsorption isotherm supports the hypothesis that the bicarbonate adsorption onto the gypsum crystals is a plausible mechanism for the retardation of the surface gypsum crystal development.

The mass accumulations of the gypsum scale with time under different supersaturation conditions are plotted in Fig. 18. Simulation results agree well with the analytical results for the crystal mass accumulation, in which the analytical results are based on the hemisphere hypothesis of the crystal structure following Eq. (17).

The crystal growth results in terms of the equilibrium radius and the mass accumulation at different locations in the spacer filled filtration channel are obtained analytically and numerically, as shown in Fig. 19 for a simulation time of 4 h. The CP prediction result ( $\text{Re} = 97.6$ ) for the top membrane is used as the supersaturation ratio by assuming that the ions in the feed flow are fully saturated for simplicity. The analytical result is obtained by using Eq. (20) and the CP prediction data. In the crystal growth simulation, the membrane surface concentration is given by  $C_w = \text{CP} \times C_s$ , in which the original supersaturation ratio  $SI$  is

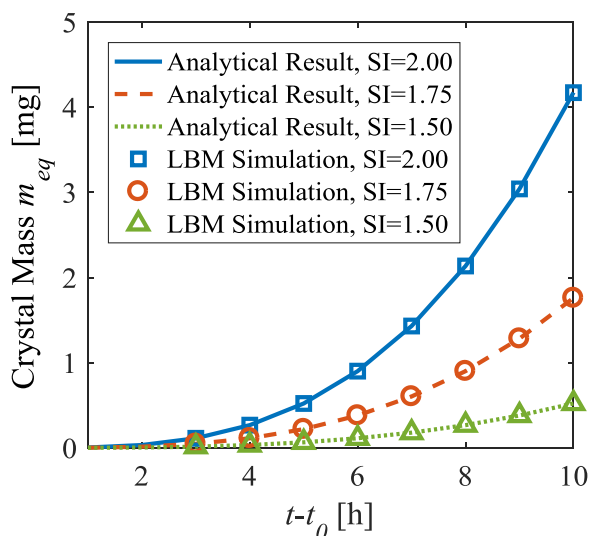


Fig. 18. Mass Accumulation of a Single Crystal.

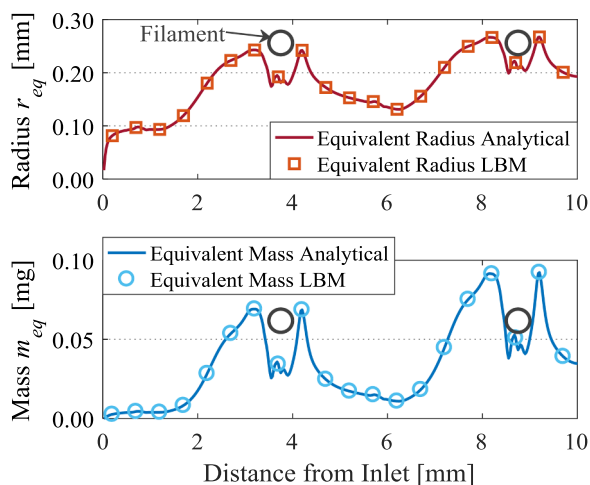


Fig. 19. Equivalent Radius and Accumulated Mass Along the Channel Length.

replaced with the predicted CP along the channel length, and  $C_s$  is the saturation concentration at a given temperature following Eq. (21). Basically, the crystal grows larger with more accumulated mass at the corner areas in front of and behind the spacer filaments along the channel length direction. The locations of the spacer filaments along the channel length direction (in  $x$ -axis) are also shown in Fig. 19.

For other saturation levels of the feed source water with respect to different ions without the fully saturation assumption, the CP prediction result can still be used to calculate the corresponding supersaturation ratio at different channel locations, since CP is a relative number between the concentration near the membrane with that in the feed flow. Numerical simulation results of the crystal growth on the membrane at the different channel locations match well with the analytical results.

#### 4. Conclusions

Concentration polarization is an inherent phenomenon in the pressure-driven membrane filtration process, which is affected by complex local hydrodynamic and thermodynamic conditions. Prediction of the solute CP is crucial for designing membrane separation modules, optimizing filtration system performance, and especially for understanding the membrane fouling phenomena. CP initiates and exacerbates membrane surface fouling. When the mineral salt concentration exceeds the saturation, mineral scaling will be formed on the membrane surface.

The currently available experimental methods for fouling observation are constrained by the module dimensions, the destructive test feature, the limited observable quantities, etc. A numerical prediction of the membrane fouling provides an alternative approach for a direct evaluation of the fouling growth, the local fluid dynamics and the concentration distribution for a wide range of operating conditions.

A lattice Boltzmann model is developed to study the CP phenomenon and the inorganic fouling growth in the pressure-driven membrane filtration process. In the CP simulation, the LBM allows a simultaneous solution of the Navier–Stokes equations and the convection-diffusion equation in a pressure-driven membrane filtration channel. The CP prediction in a plain channel is verified by comparison with published numerical data. Thereafter, the CP simulation in a spacer filled channel indicates a higher fouling potential near the spacer-membrane contact corners just in front of and behind the spacer filaments due to higher CP values in these areas. A LBM scheme for the gypsum crystal fouling growth is developed by extending the CP prediction model, which enables a direct simulation of the inorganic fouling growth at a single crystal level with respect to given solution supersaturation near the membrane surface. Both cross-flow velocity and solute concentration are lower around the formed crystal than those in the bulk flow. The predicted gypsum crystal equivalent radius and accumulated mass agree well with published experimental data and analytical results. Simulation result of the gypsum scale retardation by the bicarbonate indicates a stronger gypsum scaling retardation with increased dosage of the bicarbonate and supports the hypothesis that the bicarbonate adsorption onto the gypsum crystals is a plausible mechanism for the retardation of the surface gypsum crystal development.

The present numerical model for the membrane surface fouling growth also enables a direct evaluation of the impacts of antiscalants on the surface fouling development. It also serves as a design tool to aid in identifying suitable operating conditions for membrane filtration processes, or in the dose selection of antiscalants to mitigate inorganic fouling. Antiscalants are surface active materials that interfere with precipitation reactions primarily in ways such as keeping supersaturated solutions of sparingly soluble salts, distorting crystal shapes to get non-adherent scale, or separating crystals from solutions by adsorption. The present LB model only considers the supersaturation altering effect and the surface adsorption effect by the antiscalants, and can be used to provide initial and elementary instructions for dose selection of these mentioned types antiscalants. However, several parameters are required as inputs for the present simulation model, such as the diffusion coefficient of salts, the supersaturation ratio of solution after the antiscalant effect, the mass transfer coefficient of foulants, and the adsorption equilibrium constant of antiscalants, to predict the CP and fouling formation with antiscalants added. The current model is limited by the availability of the required input parameters for some commercial antiscalants, and by not considering the inherent interactions between different antiscalants, or other chemical effects. A more comprehensive model will better instruct desalination antiscalant dose selection, and the current numerical study should be viewed as a significant step in that development.

Future studies may involve the simulation of the crystal nucleation, which is the basis of the crystal growth study for multiple crystals as well as the membrane surface coverage by these crystals. Modeling of permeate flux decline with time and predicting the effects of fouling mitigation strategies based on the present model can also be prospective topics.

#### Acknowledgements

The authors of the paper would like to acknowledge the financial support from the Qatar National Research Fund (NPRP No.: 6–213–2–090, Centrifugal Pressure Vibrating Membrane Reverse Osmosis Desalination and Fracking Waste Water Recovery).

## Appendix A. Conversion between physical units and LBM units

In the lattice Boltzmann method, time steps and lattice spacing are usually selected as a unit 1, thus it is convenient to use dimensionless values of all the parameters. Also, some special dimensionless numbers are frequently used to characterize solutions of the Navier-Stokes equations and the convection-diffusion equation. Generally, flows with the same Reynolds number ( $Re = uL/\nu$ ) are equivalent, and solutions with the same Schmidt number ( $Sc = \nu/D$ ) are equivalent. For each physical quantity,  $Q$ , one can write:

$$Q = \bar{Q} \times C_Q \quad (A1)$$

in which

- $Q$ : physical value, include unit,  $[Q]$ ;
- $\bar{Q}$ : dimensionless value,  $[\bar{Q}] = 1$ ;
- $C_Q$ : conversion factor, include unit,  $[C_Q] = [Q]$ .

The dimensionless numbers should generally be invariant in the conversion of physical units and LBM units. Flows with the same  $Re$  and  $Sc$  are equivalent, thus

$$Re = \bar{Re} \Leftrightarrow C_{Re} \doteq 1 \quad (A2)$$

The following procedures can provide a guide of the conversion between physical units and LBM units in the desalination application (in the following, a parameter symbol with a overhead bar denotes a dimensionless parameter).

### (1) General input parameters

- Channel height:  $H = 1 \times 10^{-3}$  [m];
- Viscosity of water:  $\nu = 1.00 \times 10^{-6}$  [m<sup>2</sup>/s];
- Density of water:  $\rho = 1 \times 10^3$  [kg/m<sup>3</sup>];

### (2) LBM resolution, node number in height direction $H_{LBM} = 100$ ;

- Conversion factor of length:  $C_H = H/H_{LBM}$ , [m];

### (3) LBM density is generally selected to be: $\rho_{LBM} = 1$ ;

- Conversion factor of density:  $C_\rho = \rho/\rho_{LBM}$ , [kg/m<sup>3</sup>];

### (4) Relaxation time: $\tau = 1$ ;

For convenience, we choose the lattice spacing and the time step as:  $\bar{\Delta x} = 1$ ;  $\bar{\Delta t} = 1 \Rightarrow c = \bar{\Delta x}/\bar{\Delta t} = 1$ .

The dimensionless viscosity can be calculated as  $\bar{\nu} = (\tau - 1/2)c^2\bar{\Delta t}/3$ , and the physical unit of kinematic viscosity  $\nu$  is m<sup>2</sup>/s, thus

$$C_\nu = \frac{C_H^2}{C_T} = \frac{\nu}{\bar{\nu}} = \frac{\nu}{(\tau - 1/2)\bar{\Delta x}^2/3\bar{\Delta t}} \Rightarrow C_T = \frac{(\tau - 1/2)\bar{\Delta x}^2}{3\bar{\Delta t}} \frac{C_H^2}{\nu} \quad (A3)$$

### (5) Conversion factor of velocity: $C_U = C_H/C_T$ ;

### (6) Conversion factor of force per volume: $C_F = C_\rho C_H/C_T^2$ ;

### (7) LBM velocity:

$$\bar{U} = U/C_U \quad (A4)$$

Numerical restrictions: LBM velocity should be small (in the order of 0.1) for valid LBM simulations.

### (8) Schmidt number: $Sc = \nu/D$

### (9) Diffusion coefficient: $\bar{D} = \frac{\nu}{Sc}$ (Re and Sc are invariant in unit conversion);

### (10) Relaxation time for solute:

$$\bar{D} = (\tau_s - 1/2)c^2\bar{\Delta t}/3 \Rightarrow \tau_s = \frac{3\bar{D}\bar{\Delta t}}{\bar{\Delta x}^2} + \frac{1}{2} \quad (A5)$$

Usually, relaxation times  $\tau$  and  $\tau_s$  shall both be at least 0.55 for better stability. Usually, LBM Mach number is larger than in reality due to smaller sound speed in LBM otherwise the simulations would be too expensive. Lattice Boltzmann simulates incompressible flow under the condition of low Mach number condition ( $Ma = u/c_s < 0.3$ , where  $u$  is the macroscopic flow velocity and  $c_s$  is the speed of sound) with a weak variation in density.

## References

- [1] M.F.A. Goosen, S.S. Sablani, H. Al-Hinai, S. Al-Obeidani, R. Al-Belushi, D. Jackson, Fouling of reverse osmosis and ultrafiltration membranes: a critical review, *Sep. Sci. Technol.* 39 (2004) 2261–2297, <https://doi.org/10.1081/SS-120039343>.
- [2] A. Antony, J.H. Low, S. Gray, A.E. Childress, P. Le-Clech, G. Leslie, Scale formation and control in high pressure membrane water treatment systems: a review, *J. Memb. Sci.* 383 (2011) 1–16, <https://doi.org/10.1016/j.memsci.2011.08.054>.
- [3] S. Shirazi, C.J. Lin, D. Chen, Inorganic fouling of pressure-driven membrane processes - A critical review, *Desalination* 250 (2010) 236–248, <https://doi.org/10.1016/j.desal.2009.02.056>.
- [4] W. Guo, H.H. Ngo, J. Li, A mini-review on membrane fouling, *Bioresour. Technol.* 122 (2012) 27–34, <https://doi.org/10.1016/j.biortech.2012.04.089>.
- [5] W. Gao, H. Liang, J. Ma, M. Han, Z. Lin Chen, Z. Shuang Han, et al., Membrane fouling control in ultrafiltration technology for drinking water production: a review, *Desalination* 272 (2011) 1–8, <https://doi.org/10.1016/j.desal.2011.01.051>.
- [6] C.Y. Tang, T.H. Chong, A.G. Fane, Colloidal interactions and fouling of NF and RO

- membranes: a review, *Adv. Colloid Interface Sci.* 164 (2011) 126–143, <https://doi.org/10.1016/j.cis.2010.10.007>.
- [7] C.R. Bouchard, P.J. Carreau, T. Matsuura, S. Sourirajan, Modeling of ultrafiltration: predictions of concentration polarization effects, *J. Memb. Sci.* 97 (1994) 215–229, [https://doi.org/10.1016/0376-7388\(94\)00164-T](https://doi.org/10.1016/0376-7388(94)00164-T).
- [8] S. Kim, E.M.V. Hoek, Modeling concentration polarization in reverse osmosis processes, *Desalination* 186 (2005) 111–128, <https://doi.org/10.1016/j.desal.2005.05.017>.
- [9] A.L. Zydney, Stagnant film model for concentration polarization in membrane systems, *J. Memb. Sci.* 130 (1997) 275–281, [https://doi.org/10.1016/S0376-7388\(97\)00006-9](https://doi.org/10.1016/S0376-7388(97)00006-9).
- [10] P.L.T. Brian, Concentration polarization in reverse osmosis desalination with variable flux and incomplete salt rejection, *Ind. Eng. Chem. Fundam.* 4 (1965) 439–445, <https://doi.org/10.1021/i160016a014>.
- [11] D. Bhattacharyya, S.L. Back, R.I. Kermode, M.C. Roco, Prediction of concentration polarization and flux behavior in reverse osmosis by numerical analysis, *J. Memb. Sci.* 48 (1990) 231–262, [https://doi.org/10.1016/0376-7388\(90\)85007-8](https://doi.org/10.1016/0376-7388(90)85007-8).
- [12] A.S. Berman, Laminar flow in channels with porous walls, *J. Appl. Phys.* 24 (1953) 1232–1235, <https://doi.org/10.1063/1.1721476>.
- [13] F. Li, W. Meindersma, A.B. De Haan, T. Reith, Optimization of commercial net spacers in spiral wound membrane modules, *J. Memb. Sci.* 208 (2002) 289–302, [https://doi.org/10.1016/S0376-7388\(02\)00307-1](https://doi.org/10.1016/S0376-7388(02)00307-1).
- [14] A. Subramani, S. Kim, E.M.V. Hoek, Pressure, flow, and concentration profiles in open and spacer-filled membrane channels, *J. Memb. Sci.* 277 (2006) 7–17, <https://doi.org/10.1016/j.memsci.2005.10.021>.
- [15] M. Shakaib, S.M.F. Hasani, M. Mahmood, Study on the effects of spacer geometry in membrane feed channels using three-dimensional computational flow modeling, *J. Memb. Sci.* 297 (2007) 74–89, <https://doi.org/10.1016/j.memsci.2007.03.010>.
- [16] S. Ma, L. Song, S.L. Ong, W.J. Ng, A 2-D streamline upwind Petrov/Galerkin finite element model for concentration polarization in spiral wound reverse osmosis modules, *J. Memb. Sci.* 244 (2004) 129–139, <https://doi.org/10.1016/j.memsci.2004.06.048>.
- [17] L. Song, S. Ma, Numerical studies of the impact of spacer geometry on concentration polarization in spiral wound membrane modules, *Ind. Eng. Chem. Res.* 44 (2005) 7638–7645, <https://doi.org/10.1021/ie048795w>.
- [18] J. Kromkamp, A. Bastiaanse, J. Swarts, G. Brans, R.G.M. Van Der Sman, R.M. Boom, A suspension flow model for hydrodynamics and concentration polarisation in crossflow microfiltration, *J. Memb. Sci.* 253 (2005) 67–79, <https://doi.org/10.1016/j.memsci.2004.12.028>.
- [19] A. Rahardianto, W.Y. Shih, R.W. Lee, Y. Cohen, Diagnostic characterization of gypsum scale formation and control in RO membrane desalination of brackish water, *J. Memb. Sci.* 279 (2006) 655–668, <https://doi.org/10.1016/j.memsci.2005.12.059>.
- [20] E. Lyster, M. man Kim, J. Au, Y. Cohen, A method for evaluating antiscalant retardation of crystal nucleation and growth on RO membranes, *J. Memb. Sci.* 364 (2010) 122–131, <https://doi.org/10.1016/j.memsci.2010.08.020>.
- [21] M. Uchymiak, A. Rahardianto, E. Lyster, J. Glater, Y. Cohen, A novel RO ex situ scale observation detector (EXSOD) for mineral scale characterization and early detection, *J. Memb. Sci.* 291 (2007) 86–95, <https://doi.org/10.1016/j.memsci.2006.12.038>.
- [22] A.I. Radu, L. Bergwerff, M.C.M. van Loosdrecht, C. Picioreanu, A two-dimensional mechanistic model for scaling in spiral wound membrane systems, *Chem. Eng. J.* 241 (2014) 77–91, <https://doi.org/10.1016/j.cej.2013.12.021>.
- [23] D.A.G. Von Der Schulenburg, T.R.R. Pintelon, C. Picioreanu, M.C.M. Van Loosdrecht, M.L. Johns, Three-dimensional simulations of biofilm growth in porous media, *AIChE J.* 55 (2009) 494–504, <https://doi.org/10.1002/aic.11674>.
- [24] T. Zhang, B. Shi, Z. Guo, Z. Chai, J. Lu, General bounce-back scheme for concentration boundary condition in the lattice-Boltzmann method, *Phys. Rev. E - Stat. Nonlinear, Soft Matter Phys.* 85 (2012) 1–14, <https://doi.org/10.1103/PhysRevE.85.016701>.
- [25] Q. Chen, X. Zhang, J. Zhang, Improved treatments for general boundary conditions in the lattice Boltzmann method for convection-diffusion and heat transfer processes, *Phys. Rev. E.* 88 (2013) 033304, <https://doi.org/10.1103/PhysRevE.88.033304>.
- [26] Z. Guo, T.S. Zhao, Lattice Boltzmann model for incompressible flows through porous media, *Phys. Rev. E - Stat. Nonlinear, Soft Matter Phys.* 66 (2002), <https://doi.org/10.1103/PhysRevE.66.036304>.
- [27] M. Yoshino, T. Inamura, Lattice Boltzmann simulations for flow and heat/mass transfer problems in a three-dimensional porous structure, *Int. J. Numer. Methods Fluids* 43 (2003) 183–198, <https://doi.org/10.1002/flid.607>.
- [28] S. Chen, G. Doolen, Lattice boltzmann method for fluid flows, *Annu. Rev. Fluid Mech.* 30 (1998) 329–364, <https://doi.org/10.1007/978-3-540-27982-2>.
- [29] R. Huang, H. Wu, A modified multiple-relaxation-time lattice Boltzmann model for convection-diffusion equation, *J. Comput. Phys.* 274 (2014) 50–63, <https://doi.org/10.1016/j.jcp.2014.05.041>.
- [30] M. Li, T. Bui, S. Chao, Three-dimensional, CFD analysis of hydrodynamics and concentration polarization in an industrial RO feed channel, *Desalination* 397 (2016) 194–204, <https://doi.org/10.1016/j.desal.2016.07.005>.
- [31] Q. Zou, X. He, On pressure and velocity boundary conditions for the lattice Boltzmann BGK model, *Phys. Fluids* 9 (1997) 1591, <https://doi.org/10.1063/1.869307>.
- [32] Z. Guo, C. Zheng, B. Shi, Discrete lattice effects on the forcing term in the lattice Boltzmann method, *Phys. Rev. E.* 65 (2002) 046308, <https://doi.org/10.1103/PhysRevE.65.046308>.
- [33] R. Bian, K. Yamamoto, Y. Watanabe, The effect of shear rate on controlling the concentration polarization and membrane fouling, *Desalination* 131 (2000) 225–236, [https://doi.org/10.1016/S0011-9164\(00\)90021-3](https://doi.org/10.1016/S0011-9164(00)90021-3).
- [34] H.-B. Huang, X.-Y. Lu, M.C. Sukop, Numerical study of lattice Boltzmann methods for a convection–diffusion equation coupled with Navier–Stokes equations, *J. Phys. A Math. Theor.* 44 (2011) 055001, <https://doi.org/10.1088/1751-8113/44/5/055001>.
- [35] Y. Lee, M.M. Clark, Modeling of flux decline during crossflow ultrafiltration of colloidal suspensions, *J. Memb. Sci.* 149 (1998) 181–202, [https://doi.org/10.1016/S0376-7388\(98\)00177-X](https://doi.org/10.1016/S0376-7388(98)00177-X).
- [36] A. Poisson, A. Papaud, Diffusion coefficients of major ions in seawater, *Mar. Chem.* 13 (1983) 265–280, [https://doi.org/10.1016/0304-4203\(83\)90002-6](https://doi.org/10.1016/0304-4203(83)90002-6).
- [37] J. Perko, R.A. Patel, Single-relaxation-time lattice Boltzmann scheme for advection-diffusion problems with large diffusion-coefficient heterogeneities and high-advection transport, *Phys. Rev. E - Stat. Nonlinear, Soft Matter Phys.* 89 (2014) 1–9, <https://doi.org/10.1103/PhysRevE.89.053309>.
- [38] Q. Kang, D. Zhang, P.C. Lichtner, I.N. Tsimpanogiannis, Lattice Boltzmann model for crystal growth from supersaturated solution, *Geophys. Res. Lett.* 31 (2004) 1–5, <https://doi.org/10.1029/2004GL021107>.
- [39] M. Uchymiak, E. Lyster, J. Glater, Y. Cohen, Kinetics of gypsum crystal growth on a reverse osmosis membrane, *J. Memb. Sci.* 314 (2008) 163–172, <https://doi.org/10.1016/j.memsci.2008.01.041>.
- [40] W.Y. Shih, A. Rahardianto, R.W. Lee, Y. Cohen, Morphometric characterization of calcium sulfate dihydrate (gypsum) scale on reverse osmosis membranes, *J. Memb. Sci.* 252 (2005) 253–263, <https://doi.org/10.1016/j.memsci.2004.12.023>.
- [41] H. Oh, Y. Choung, S. Lee, J. Choi, T. Hwang, J. Kim, Scale formation in reverse osmosis desalination: model development, *Desalination* 238 (2009) 333–346, <https://doi.org/10.1016/j.desal.2008.10.005>.
- [42] F. Alimi, A. Gadjri, Kinetics and morphology of formed gypsum, *Desalination* 166 (2004) 427–434, <https://doi.org/10.1016/j.desal.2004.06.097>.
- [43] P. Dydo, M. Turek, J. Ciba, K. Wandachowicz, J. Misztal, The nucleation kinetic aspects of gypsum nanofiltration membrane scaling, *Desalination* 164 (2004) 41–52, [https://doi.org/10.1016/S0011-9164\(04\)00154-7](https://doi.org/10.1016/S0011-9164(04)00154-7).
- [44] M. Brusilovsky, J. Borden, D. Hasson, Flux decline due to gypsum precipitation on RO membranes, *Desalination* 86 (1992) 187–222, [https://doi.org/10.1016/0011-9164\(92\)80033-6](https://doi.org/10.1016/0011-9164(92)80033-6).
- [45] S. Lee, C.H. Lee, Effect of operating conditions on CaSO<sub>4</sub> scale formation mechanism in nanofiltration for water softening, *Water Res.* 34 (2000) 3854–3866, [https://doi.org/10.1016/S0043-1354\(00\)00142-1](https://doi.org/10.1016/S0043-1354(00)00142-1).
- [46] E. Fountoukidis, Z.B. Maroulis, D. Marinos-Kouris, Crystallization of calcium sulfate on reverse osmosis membranes, *Desalination* 79 (1990) 47–63, [https://doi.org/10.1016/0011-9164\(90\)80070-R](https://doi.org/10.1016/0011-9164(90)80070-R).
- [47] A. Rahardianto, B.C. Mccool, Y. Cohen, Reverse osmosis desalting of inland brackish water of high gypsum scaling propensity: kinetics and mitigation of membrane mineral scaling, *Environ. Sci. Technol.* 42 (2008) 4292–4297, <https://doi.org/10.1021/es702463a>.
- [48] W. Li, X. Su, A. Palazzolo, S. Ahmed, E. Thomas, Reverse osmosis membrane, seawater desalination with vibration assisted reduced inorganic fouling, *Desalination* 417 (2017) 102–114, <https://doi.org/10.1016/j.desal.2017.05.016>.
- [49] K.J. Kim, A. Mersmann, Estimation of metastable zone width in different nucleation processes, *Chem. Eng. Sci.* 56 (2001) 2315–2324, [https://doi.org/10.1016/S0009-2509\(00\)00450-4](https://doi.org/10.1016/S0009-2509(00)00450-4).